

Article

# Effect of Calcination Conditions on the Properties and Photoactivity of TiO<sub>2</sub> Modified with Biuret

Aleksandra Piątkowska  and Sylwia Mozia \* 

Department of Inorganic Chemical Technology and Environment Engineering, Faculty of Chemical Technology and Engineering, West Pomeranian University of Technology in Szczecin, ul. Pułaskiego 10, 70-322 Szczecin, Poland; aleksandra.piatkowska@zut.edu.pl

\* Correspondence: sylwia.mozia@zut.edu.pl; Tel.: +48-91-449-4730

**Abstract:** A simple wet impregnation-calcination method was used to obtain a series of novel non-metal doped TiO<sub>2</sub> photocatalysts. Biuret was applied as C and N source, while raw titanium dioxide derived from sulfate technology process was used as TiO<sub>2</sub> and S source. The influence of the modification with biuret and the effect of the atmosphere (air or argon) and temperature (500–800 °C) of calcination on the physicochemical properties and photocatalytic activity of the photocatalysts towards ketoprofen decomposition under simulated solar light was investigated. Moreover, selected photocatalysts were applied for ketoprofen photodecomposition under visible and UV irradiation. Crucial features affecting the photocatalytic activity were the anatase to rutile phase ratio, anatase crystallites size and non-metals content. The obtained photocatalysts revealed improved activity in the photocatalytic ketoprofen decomposition compared to the crude TiO<sub>2</sub>. The best photoactivity under all irradiation types exhibited the photocatalyst calcined in the air atmosphere at 600 °C, composed of 96.4% of anatase with 23 nm crystallites, and containing 0.11 wt% of C, 0.05 wt% of N and 0.77 wt% of S.

**Keywords:** TiO<sub>2</sub>; carbon; nitrogen; sulfur; photocatalysis; ketoprofen



**Citation:** Piątkowska, A.; Mozia, S. Effect of Calcination Conditions on the Properties and Photoactivity of TiO<sub>2</sub> Modified with Biuret. *Catalysts* **2021**, *11*, 1546. <https://doi.org/10.3390/catal11121546>

Academic Editors: Detlef W. Bahnemann, Ewa Kowalska, Ioannis Konstantinou, Magdalena Janus, Vincenzo Vaiano, Wonyong Choi and Zhi Jiang

Received: 24 November 2021

Accepted: 15 December 2021

Published: 18 December 2021

**Publisher's Note:** MDPI stays neutral with regard to jurisdictional claims in published maps and institutional affiliations.



**Copyright:** © 2021 by the authors. Licensee MDPI, Basel, Switzerland. This article is an open access article distributed under the terms and conditions of the Creative Commons Attribution (CC BY) license (<https://creativecommons.org/licenses/by/4.0/>).

## 1. Introduction

Water scarcities and water pollution are becoming one of the greatest environmental threats of the 21st century. Over one billion people do not have access to drinking water [1]. Rapid industrialization and growing production lead to the increase in the presence of organic pollutants in the water environment each year. A significant part of these pollutions are pharmaceuticals. The first discovery of pharmaceutically active compounds in aquatic systems occurred in 1980s [2]. Studies show that over 100 pharmaceutical compounds from different therapeutic classes have been detected in wastewater, but also in drinking and ground water around the world [3,4]. Pharmaceuticals have been proved to have high potential threat for ecosystems and human as well as animal health [5,6]. Globally non-steroidal anti-inflammatory drugs (NSAIDs) are among the most frequently detected medications in surface waters. This is due to the high availability and no medical prescription requirements for these supplies [2,7–9]. In the example of ketoprofen, the concentration detected in natural environment ranged from 16 ng/L in drinking water in Europe, even to 9220 ng/L in surface water in Africa [2]. It means that pharmaceuticals could be introduced into the human body unintentionally by consuming drinking water [6,7,10–12].

Numerous studies showed that conventional wastewater treatment plants based on the use of microorganisms are insufficient to remove pharmaceuticals because of their complex molecular structure and good stability [4]. Due to that, the interest of many researchers has focused on the development of new, effective methods of removing these pollutants from the aquatic environment [5,13,14]. It has been proven that photocatalysis is an effective method of decomposition and mineralization of organic pollutants, including pharmaceuticals [2,5,13]. In the photocatalytic process a photocatalyst, e.g., TiO<sub>2</sub> absorbs

the radiation and causes the chemical conversion of substances involved in the reaction. The photogenerated electron-hole pairs participate in a series of reactions leading to the production of various reactive oxygen species (ROS), including the extremely strong oxidant  $\bullet\text{OH}$ , which have the ability to decompose organic compounds [15–17]. The final products of photocatalytic mineralization of organic compounds are  $\text{CO}_2$ ,  $\text{H}_2\text{O}$  and inorganic ions.

Amongst various semiconductors,  $\text{TiO}_2$  is the most commonly applied in photocatalysis. Its main advantages are low cost and good chemical stability. However, it also suffers from several weaknesses including low intrinsic electron mobility ( $0.1\text{--}1\text{ cm}^2/\text{V}\cdot\text{s}$ ) and high sintering temperature ( $>450\text{ }^\circ\text{C}$ ) [18–20]. Nonetheless, its main disadvantage is the need to be activated with the use of UV radiation. Hence, numerous methods of modifying  $\text{TiO}_2$  are being investigated [15,21,22]. One of the approaches to increase the photocatalytic activity in visible light is non-metal doping. Modification of  $\text{TiO}_2$  with non-metals causes changes in the structure of the electron bands, generally leading to a decrease in the band gap energy [21–23]. Carbon, nitrogen and sulfur seem to be very feasible dopants [24–26]. The most common non-metals sources include urea [27,28], thiourea [29], ammonia [30,31] and glucose [32,33]. The non-metal doping of  $\text{TiO}_2$  usually results in narrowing of the band gap due to the formation of new impurity levels (e.g., C 2p, N 2p, S 2p) above the valence band (VB) of the semiconductor [34–36]. The incorporation of the heteroatoms can be confirmed on a basis of X-ray photoelectron spectroscopy (XPS) analysis [37,38]. N-doping is the most common non-metal doping method. It can be conducted either interstitially by incorporating nitrogen atoms into  $\text{TiO}_2$  lattice or substitutionally by replacing oxygen with nitrogen [39,40]. The researchers seem to disagree about which N-doping mode provides with better results [41,42]. Doping of  $\text{TiO}_2$  with carbon atoms can result in: (i) formation of Ti-C bonds due to the substitution of lattice oxygen with C, (ii) replacement of Ti by C leading to the formation of C-O bonds, or (iii) stabilization of C at the interstitial position [43,44]. Sulfur in the S-doped  $\text{TiO}_2$  can be incorporated through two paths, cationic or anionic. Cationic doping occurs by titanium substitution with  $\text{S}^{6+}$  cation, while anionic doping takes place by oxygen substitution with  $\text{S}^{2-}$  anion [45–48]. Each individual non-metal doping mode has some advantages and disadvantages. Therefore, co-doping and tri-doping of  $\text{TiO}_2$  with non-metals was proposed, leading to combinations of the properties of single-doped  $\text{TiO}_2$  [49–51]. Further details on the C-, N-, S- as well as co-doped and tri-doped  $\text{TiO}_2$  can be found elsewhere [37].

In the present paper, a new approach to the modification of  $\text{TiO}_2$  with non-metals such as C, N and S is proposed.  $\text{TiO}_2$  from sulfate technology and biuret were used for the preparation of the photocatalysts. Unlike other frequently applied  $\text{TiO}_2$  precursors, such as titanium(IV) isopropoxide [52,53], titanium(IV) butoxide [54,55],  $\text{TiCl}_4$  [56] or Aeroxide<sup>®</sup>  $\text{TiO}_2$  P25 [57], the  $\text{TiO}_2$  from the sulfate technology offers an advantage of being a source of  $\text{TiO}_2$  and sulfur simultaneously. Furthermore, to the best of our knowledge biuret has not been used for the purpose of  $\text{TiO}_2$  modification with C and N ever before. Another aspect of novelty relates to the evaluation of the influence of the calcination atmosphere on the physicochemical properties and photocatalytic activity of the modified  $\text{TiO}_2$ . There are very few reports in which the influence of the atmosphere of the heat treatment on the non-metal doped photocatalyst performance had been investigated and none of them refers to the comparison of the effect of the air and argon atmosphere [58–62].

Taking the above into consideration, the aim of the presented research was to investigate the influence of the modification of  $\text{TiO}_2$  with non-metals such as C, N and S on its physicochemical properties and photocatalytic activity under simulated solar light, as well as visible ( $>470\text{ nm}$ ) and UV radiation. The effect of the calcination atmosphere (air and argon) and temperature ( $500\text{--}800\text{ }^\circ\text{C}$ ), as well as biuret amount was especially examined. Wet impregnation-calcination approach was applied for the photocatalyst preparation. The photocatalytic activity was evaluated based on the degradation of a commonly used NSAID, ketoprofen.

## 2. Experimental Section

### 2.1. Materials

All chemicals were used as received without further purification. Crude TiO<sub>2</sub> produced by the sulfate technology was supplied by the Grupa Azoty Zakłady Chemiczne "Police" S.A. (Police, Poland). Biuret and ketoprofen were purchased from Sigma-Aldrich (Saint Louis, MO, USA).

### 2.2. Photocatalysts Synthesis

The photocatalysts were prepared by a simple wet impregnation-calcination approach. Biuret and crude TiO<sub>2</sub> were mixed at the TiO<sub>2</sub>:N weight ratio of 9.8:0.2, 9.7:0.3, 9.5:0.5, 9:1, 7:3 or 5:5 and suspended in 100 mL of ultrapure water. The suspensions were stirred at room temperature for 18 h. Subsequently, the samples were dried at 105 °C to evaporate water. The obtained products were ground in an agate mortar to form a fine powder. Finally, the dry powders were calcined for 1 h in the air or argon atmosphere at 500, 600, 700 or 800 °C with a heating rate of 5 °C/min. For argon, the gas flow was 50 mL/min. The obtained photocatalysts were labeled as B-X-P/Ar-Y, where X denoted the TiO<sub>2</sub>:N ratio, P was for air, Ar was for argon and Y denoted the calcination temperature (°C).

### 2.3. Photocatalysts Characterization

The crystalline structure of the photocatalysts was characterized by the X-ray diffraction (XRD, PANalytical Empyrean, CuK $\alpha$  radiation  $\lambda = 1.54056 \text{ \AA}$ ). The average anatase crystallite sizes were calculated using Scherrer formula [63,64]:

$$D = \frac{K\lambda}{W \cos \theta} \quad (1)$$

in which K is a numerical constant ( $K = 0.93$ ),  $\lambda$  is the CuK $\alpha$  radiation wavelength ( $\lambda = 1.54056 \text{ \AA}$ ), W is the full width at half maximum of the diffraction lines (FWHM) and  $\theta$  is the diffraction angle. The W parameter was calculated based on the following equation:

$$W = \sqrt{(W_0 - W_1) \cdot \sqrt{W_0^2 - W_1^2}} \quad (2)$$

where  $W_0$  is the measured value and  $W_1$  is the instrument correction factor.

The UV-Vis/DR spectra of the crude TiO<sub>2</sub> and the prepared photocatalysts were measured in the scan range of 200–800 nm using UV-Vis/DR spectrophotometer (Jasco V-650, Tokyo, Japan). Spectralon white diffuse reflectance standard was used as a reference. In order to calculate the band gap energy, the linear part of the Tauc plot was extrapolated. The Tauc method is based on the following formula:

$$(\alpha \cdot h\nu)^{1/\gamma} = B(h\nu - E_g) \quad (3)$$

where  $\alpha$  is an energy-dependent absorption coefficient, h is the Planck constant,  $\nu$  is the photon frequency,  $\gamma$  is the factor dependent on the nature of the electron transition, B is a constant and  $E_g$  is the band gap energy. The  $\gamma$  factor is equal to 1/2 and 2 for the direct and indirect transition, respectively [65]. The intersection with the OX axis indicates the band gap energy value.

Carbon, nitrogen and sulfur content were analyzed with the use of elemental analyzers (CS230 and ONH836 Leco Corp., St. Joseph, MO, USA). The isoelectric point (pH(I)) was determined using the Zetasizer Nano-ZS analyzer (Malvern Instruments Ltd., Malvern, UK).

### 2.4. Photocatalytic Reaction

The photocatalytic activity of the obtained materials was determined based on the decomposition of ketoprofen in the presence of simulated solar light. An amount of

10 mg/L ketoprofen solution in ultrapure water was used as a model pollutant. The concentration of photocatalyst in the reaction suspension was 1 g/L. The process was carried out in a test system separated from the outer radiation. The system consisted of a beaker with a cooling jacket, placed on a magnetic stirrer and a 150 W light bulb (Daylight Basking Spot, Exo Terra), which simulated solar radiation. The radiation intensity was measured with a radiometer (LB-901, LAB-EL, Warsaw, Poland) equipped with two external sensors. The first one was a pyranometer (CMP3, Kipp & Zonen, Delft, The Netherlands) with the spectral range of 300 to 2800 nm. The second one was a UV sensor (PD204AB Cos, Macam Photometrics Ltd., Livingston, NJ, USA) with the spectral range of UV-A and UV-B ( $\lambda_{\max} = 352$  nm, band width:  $79 \pm 4$  nm). The measured radiation intensity was ca.  $1250 \text{ W/m}^2$  in the wavelength range of 300–2800 nm and  $0.4 \text{ W/m}^2$  in the wavelength range of UV-A and UV-B. The temperature was kept at  $20 \text{ }^\circ\text{C} \pm 1 \text{ }^\circ\text{C}$ . The photocatalysis process was preceded by an hour-long adsorption in the dark to ensure the adsorption-desorption equilibrium. After this stage, the lamp was turned on and the photocatalysis process was carried out for 24 h. The samples were collected every hour for the first 5 h and then one sample was taken after 24 h. The samples were filtered through a  $0.45 \text{ }\mu\text{m}$  nylon syringe filter to separate the photocatalyst. Each experiment was repeated at least two times to confirm the reproducibility of the results.

The concentration of ketoprofen was measured using high performance liquid chromatograph (HPLC, Shimadzu, Kyoto, Japan) equipped with a Purospher® STAR RP-18 endcapped 250–4 column and SPD-M40 photo diode array detector. The mobile phase consisted of 60% 20 mmol/L  $\text{Na}_2\text{HPO}_4 \cdot 2\text{H}_2\text{O}$  (pH = 2.6 adjusted with  $\text{H}_3\text{PO}_4$ ) and 40% acetonitrile. The flow rate of eluent was 1.0 mL/min. The column was thermostated at  $30 \text{ }^\circ\text{C}$ . Total organic carbon (TOC) was measured using TOC analyzer (multi N/C 2000, Analytik Jena, Jena, Germany).

For the evaluation of the photoactivity, the concentration of ketoprofen after adsorption in the dark was taken as the initial concentration. The removal efficiency was calculated using the following formula:

$$\% \text{ removal} = \frac{c_0 - c_t}{c_0} \times 100\% \quad (4)$$

where  $c_0$  was the initial ketoprofen concentration (mg/L) and  $c_t$  denoted the concentration at time  $t$  (mg/L).

The apparent pseudo-first order rate constant ( $k$ ) was calculated from the relationship:

$$r = -\frac{dc}{dt} = kc \quad (5)$$

where  $c$  is ketoprofen concentration,  $k$  is rate constant and  $t$  is time [66]. The rate constant  $k$  ( $\text{h}^{-1}$ ) was determined from the slope of the linear regression obtained by plotting  $-\ln(c_t/c_0)$  vs  $t$ .

The photocatalytic activity of selected photocatalysts was additionally investigated in the presence of visible and UV light. For visible light photocatalytic experiment, the same light bulbs were used as for the simulated solar light experiment. Moreover, the UV filter foil (METOLIGHT SFLY5, ASMETEC GmbH, Kirchheimbolanden, Germany) was applied to cut off the short wavelength components below 470 nm, which can be seen in Figure 1. The radiation intensity was ca.  $1100 \text{ W/m}^2$  in the wavelength range of 300–2800 nm. For the UV light experiment, two 20 W UV lamps (CLEO, iSOLde, Stuttgart, Germany) were used with the UV radiation intensity of ca.  $25 \text{ W/m}^2$ .

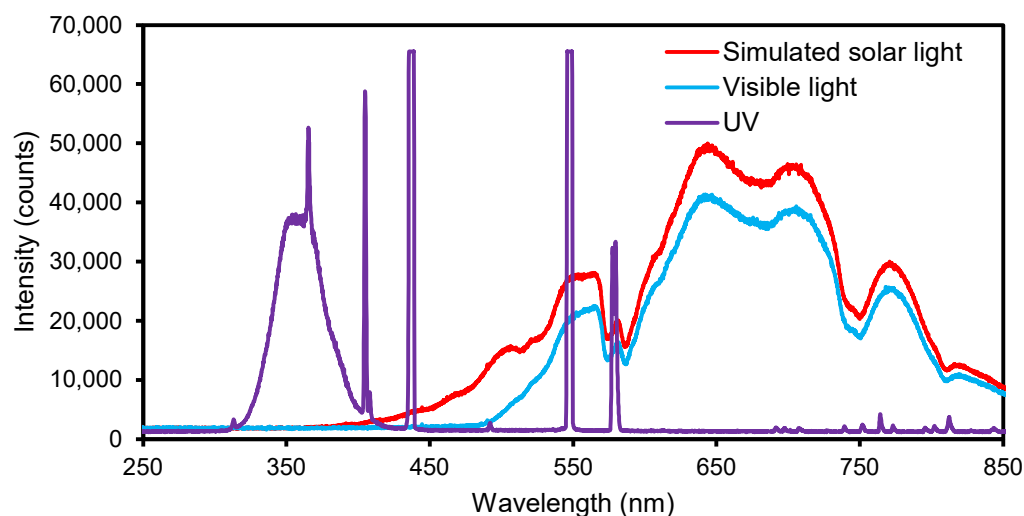


**Figure 1.** Spectral distribution of simulated solar light, visible light and UV.

### 3. Results and Discussion

#### 3.1. Physicochemical Properties of the Photocatalysts

Different photocatalysts were synthesized under variable conditions such as the  $\text{TiO}_2\text{:N}$  weight ratio, calcination atmosphere and temperature. The properties of crude and non-metal doped  $\text{TiO}_2$  are summarized in Table 1 in terms of crystal phase ratio (%), anatase crystallite size (nm), band gap energy (eV), C, N and S content (wt%) as well as isoelectric point.

The XRD patterns of the crude  $\text{TiO}_2$ , used as a reference, as well as different non-metal doped photocatalysts are shown in Figure 2. The presence of two crystalline phases, anatase and rutile, was observed. It was noticed that in the case of photocatalysts, calcined both in the air and argon atmosphere, the anatase phase content was highly dependent on the temperature used (Figure 2a,b). The crude  $\text{TiO}_2$  was mainly amorphous with some amount of poorly crystalline anatase. The photocatalysts calcined at 500 and 600 °C were characterized by a similar intensity of the anatase peaks ( $2\theta = 25.32^\circ, 36.96^\circ, 37.83^\circ, 38.60^\circ, 48.01^\circ, 53.96^\circ, 55.10^\circ, 62.74^\circ$  and  $75.12^\circ$ ), regardless of the atmosphere, which indicates similar anatase content (94.6–96.8%, Table 1). A difference can be observed in the case of the photocatalysts calcined at 700 °C. The application of air inhibited the transformation of anatase to rutile. The content of anatase in the case of B-9-1-P-700 was 92.9%, while in the case of B-9-1-Ar-700 amounted to 39.9%. A further increase in the temperature led to the increase in the intensity of rutile peaks ( $2\theta = 27.48^\circ, 36.12^\circ, 39.24^\circ, 41.28^\circ, 44.09^\circ, 54.37^\circ, 56.68^\circ, 64.10^\circ, 69.04^\circ$  and  $69.83^\circ$ ), indicating almost complete conversion of anatase for both calcination atmospheres.

Table 1. Physicochemical properties of the crude TiO<sub>2</sub> and the prepared photocatalysts.

Photocatalyst	TiO <sub>2</sub> :N Ratio	Calcination Temperature (°C)	Calcination Atmosphere	Anatase Phase Content (%)	Rutile Phase Content (%)	Anatase Crystallite Size (nm)	Band Gap Energy E <sub>g</sub> (eV)		Non-Metal Content (wt%)			Isoelectric Point pH(I)
							Indirect	Direct	C	N	S	
Crude TiO <sub>2</sub>	-	-	-	100	0	7	3.31	3.67	0.11	0.06	2.36	6.1
B-9-1-P-500	9:1	500	air	95.8	4.2	14	3.27	3.54	0.49	0.06	2.18	5.5
B-9-1-P-600	9:1	600	air	96.4	3.6	23	3.26	3.51	0.11	0.05	0.77	5.5
B-9-1-P-700	9:1	700	air	92.9	7.1	35	3.23	3.49	0.05	0.02	0.24	5.5
B-9-1-P-800	9:1	800	air	2.7	97.3	- *	3.01	3.19	0.08	0.02	0.06	3.6
B-9-1-Ar-500	9:1	500	argon	96.8	3.2	18	3.25	3.54	0.05	0.06	0.16	6.2
B-9-1-Ar-600	9:1	600	argon	94.6	5.4	26	3.21	3.46	0.07	0.03	0.10	6.4
B-9-1-Ar-700	9:1	700	argon	39.9	60.1	44	3.02	3.24	0.03	0.00	0.05	4.5
B-9-1-Ar-800	9:1	800	argon	2.5	97.5	- *	3.01	3.18	0.02	0.00	0.03	3.7
B-9.5-0.5-P-600	9.5:0.5	600	air	100	0	25	3.27	3.54	0.10	0.03	0.82	4.5
B-7-3-P-600	7:3	600	air	95.0	5.0	27	3.23	3.49	0.14	0.13	0.42	4.6
B-5-5-P-600	5:5	600	air	94.3	5.7	28	3.21	3.47	0.19	0.16	0.33	5.5
B-9.8-0.2-Ar-600	9.8:0.2	600	argon	97.1	2.9	21	3.27	3.54	0.06	0.01	0.86	5.0
B-9.7-0.3-Ar-600	9.7:0.3	600	argon	97.1	2.9	21	3.27	3.53	0.06	0.02	0.85	5.7
B-9.5-0.5-Ar-600	9.5:0.5	600	argon	97.1	2.9	22	3.26	3.53	0.07	0.02	0.83	5.5

\* It was not possible to accurately measure the size of the crystallites because the anatase reflex was not intense enough.

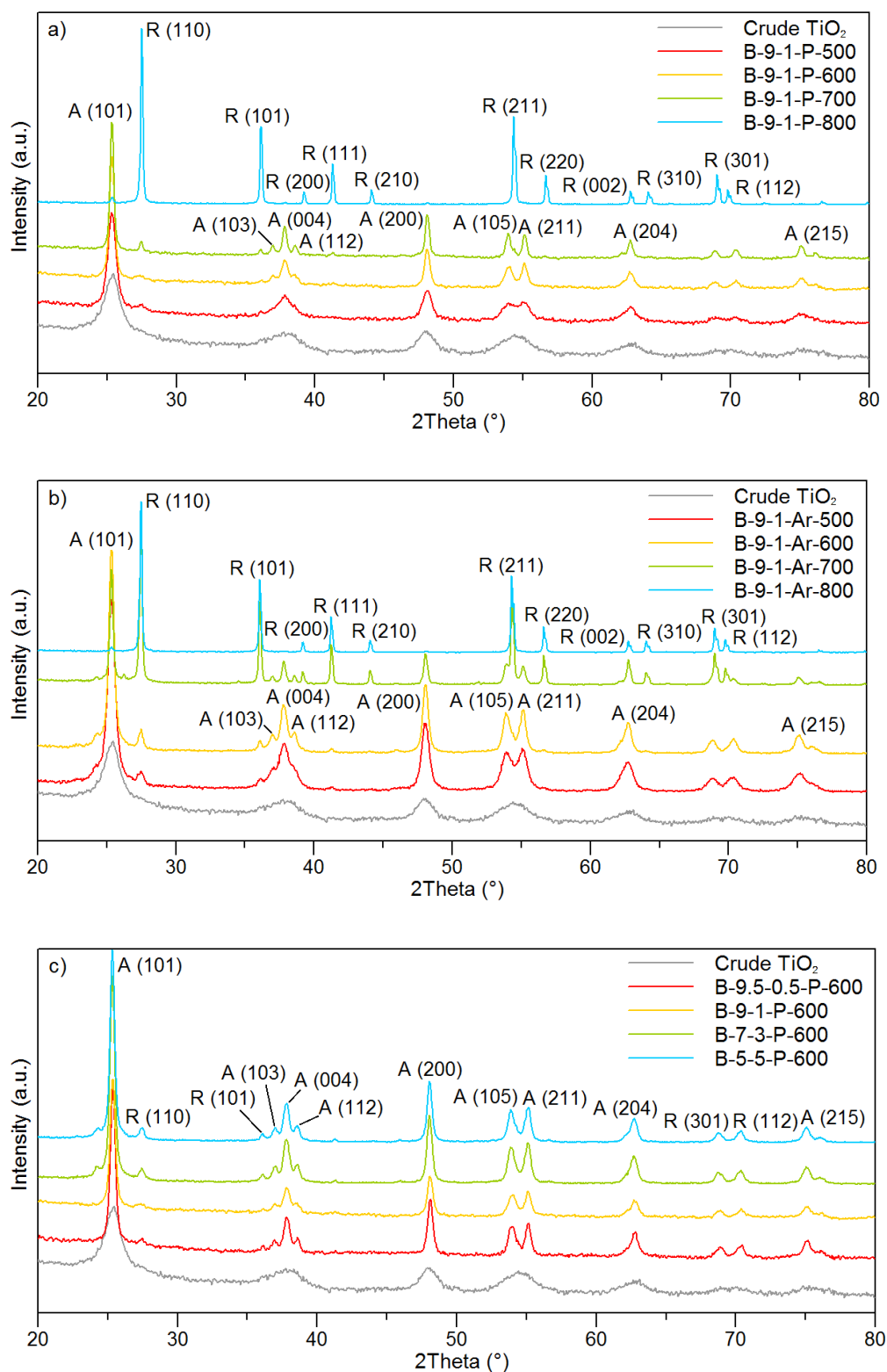
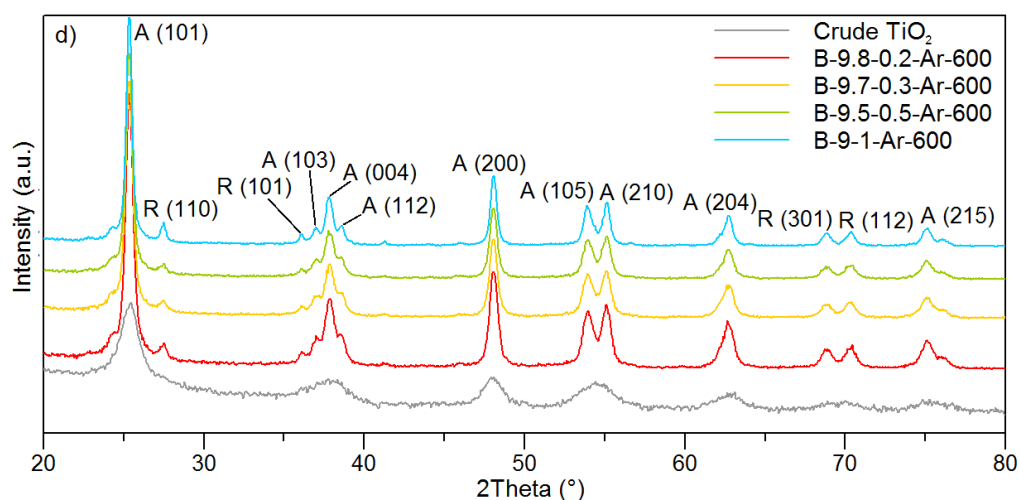


Figure 2. Cont.



**Figure 2.** XRD patterns of the crude  $\text{TiO}_2$  and photocatalysts prepared (a) with the  $\text{TiO}_2$ :N ratio of 9:1 in air and different calcination temperatures, (b) with the  $\text{TiO}_2$ :N ratio of 9:1 in argon and different calcination temperatures, (c) with different  $\text{TiO}_2$ :N ratios in air and calcined at 600 °C, (d) with different  $\text{TiO}_2$ :N ratios in argon and calcined at 600 °C.

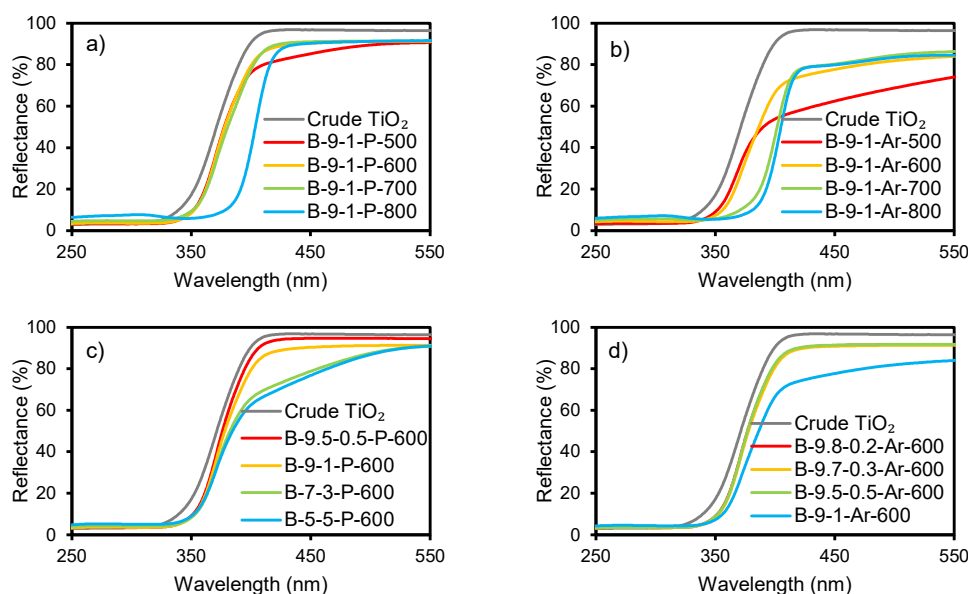
The transition from anatase to rutile is a nucleation and growth process. In general, the kinetics of the phase transformation is considered in terms of temperature and time, and depends on variables such as precursor composition (e.g., presence of impurities) and morphology, preparation method, heating conditions, etc. The transformation of anatase to rutile requires sufficient thermal energy to enable the rearrangement of atoms at a measurable rate. Pure bulk anatase is reported widely to begin to transform irreversibly to rutile in air at ~600 °C; however, the transition temperatures can vary depending on the process parameters and substrate properties [67]. According to Czanderna et al. [68], the anatase-rutile phase transformation below 610 °C is immeasurably slow, whereas above 730 °C it occurs extremely rapidly, which agrees with the obtained results for the photocatalysts calcined in air. It was revealed that the photocatalysts annealed in air at 500–700 °C consisted mostly of the anatase phase, while the photocatalyst calcined at 800 °C was composed mostly of the rutile phase. Nevertheless, the results confirmed that using the argon atmosphere leads to a decrease in the temperature of the crystalline phase transition from anatase to rutile compared to the air atmosphere. The enhancement in anatase to rutile transformation through the use of a non-oxidizing gas, such as argon is considered to be due to the increased levels of oxygen vacancies [67]. The rate of phase transformation increases with the lower oxygen partial pressure, so it happens in the argon atmosphere [69].

Figure 2c,d shows that the modification with different amounts of biuret did not affect the crystalline structure of  $\text{TiO}_2$  as much as the use of different calcination temperatures. Nonetheless, another observed change related to the temperature rise was the narrowing of peaks, which indicates an increase in the size of crystallites. The diameter of anatase crystallites determined for the biuret modified photocatalysts varied in the range from 14 nm to 44 nm. The smallest crystallites with the diameter below 20 nm were observed for the photocatalysts calcined at 500 °C both in air and argon. The use of calcination temperature of 600 °C resulted in crystallites having from 21 to 28 nm in size, whereas photocatalysts calcined at 700 °C had anatase crystallites of 35 nm and larger. However, it was not possible to accurately measure the size of the crystallites for photocatalysts calcined at 800 °C, because the anatase reflex was not intense enough. Generally, in the case of the photocatalysts calcined in the argon atmosphere, the crystallites were larger than in the case of the photocatalysts calcined at the same temperature in air. This leads to the conclusion that calcination atmosphere has an impact on the crystallite growth. Albetran et al. [70] also observed development of larger crystallites in the argon atmosphere than during the

calcination in air. The authors explained this by the oxygen vacancies created in argon, which enhanced the crystallites growth because of the increased solid state diffusion. The atomic diffusion or the cooperative titania atom rearrangements as well as the movements of the grain boundaries during the phase transition take place easier in argon than in air, due to the higher mobility of titania atoms in the presence of the oxygen vacancies. This can result in the larger size of anatase crystallites. In turn, Amores et al. [71] claimed that the additives to  $\text{TiO}_2$ , which enhance the rate of the anatase to rutile phase transformation, can also have an impact on the rate of the crystallite growth. Moreover, they discovered that the additives that inhibit the phase transition can also hinder the crystallite sintering. This can be the reason why the argon atmosphere, accelerating the anatase to rutile transformation, contributed to the anatase crystallite growth, as well. These two processes of the phase transition and the anatase crystallite growth can occur simultaneously and affect each other. The anatase to rutile transformation enhances the crystallite sintering because of the superior atomic mobility due to the bond breakage during the transformation [72].

The calcination conditions also had a significant influence on the content of the non-metals in the photocatalysts. For the photocatalysts with  $\text{TiO}_2$ :N ratio of 9:1, a decrease in the sulfur, carbon and nitrogen content with an increase in the calcination temperature can be observed for both air and argon atmosphere (Table 1). Another relationship noticeable for both calcination atmospheres was a decrease in sulfur content with increasing amount of biuret in the suspension used for the preparation of the photocatalysts calcined at 600 °C. Sulfur in the photocatalysts came from the crude  $\text{TiO}_2$ , which contains its residues from the sulfate technology process. In the case of the photocatalysts synthesized with the  $\text{TiO}_2$ :N ratio of 9.5:0.5, 9:1, 7:3 and 5:5 and calcined in air, the sulfur content was 0.82, 0.77, 0.42 and 0.33 wt%, respectively. When argon atmosphere was applied, the sulfur content was 0.86, 0.85, 0.83 and 0.10 wt%, for the  $\text{TiO}_2$ :N ratio of 9.8:0.2, 9.7:0.3, 9.5:0.5 and 9:1, respectively. An opposite relationship can be observed in the case of carbon and nitrogen content in the photocatalysts. The C and N amount increased with an increasing loading of biuret, revealing that the presence of these non-metals in the photocatalysts originated from the organic precursor. The photocatalysts prepared with the  $\text{TiO}_2$ :N ratio of 9.5:0.5, 9:1, 7:3 and 5:5, and calcined in air had the carbon content of 0.10–0.19 wt%, respectively, while the nitrogen content was in the range of 0.03–0.16 wt%, respectively. The amount of carbon and nitrogen in the case of the photocatalysts calcined in argon amounted to 0.06–0.07 wt% and 0.01–0.03 wt%, respectively. Generally, the greater amount of the non-metals was observed for the photocatalysts calcined in the air than in the argon atmosphere. This was particularly noticeable for S content.

The applied procedure of modification affected also the optical properties of the photocatalysts. Figure 3 shows the UV-Vis/DR spectra of the crude  $\text{TiO}_2$  and the non-metal doped photocatalysts calcined in the air and argon atmosphere. The spectra of all non-metal-doped photocatalysts revealed a bathochromic shift compared to the crude  $\text{TiO}_2$ . Figure 3a,b shows the influence of the calcination temperature on the reflectance spectra. The greatest shift was observed for the photocatalyst calcined at 800 °C from the series prepared in air and for the photocatalysts calcined at 700 °C and 800 °C from the series synthesized in argon. In both series, the photocatalysts calcined at 500 °C displayed a noticeable decrease in reflectance above ca. 400 nm, which can be related to their yellowish color. Furthermore, Figure 3c,d shows that the photocatalysts modified with a higher amount of biuret revealed a similar decrease in reflectance. That can be associated with a higher C and N content in the photocatalysts, as can be found from Table 1. Moreover, the introduction of larger amounts of C and N into  $\text{TiO}_2$  caused a more noticeable redshift of the absorption edge of  $\text{TiO}_2$  (Figure 3c,d). This is in agreement with the literature reports indicating that the non-metal doping introduces impurity levels above the valence band of a photocatalyst, resulting in the redshift and narrower band gap [73,74].



**Figure 3.** UV-Vis/DR spectra of the crude TiO<sub>2</sub> and photocatalysts prepared (a) in air with the TiO<sub>2</sub>:N ratio of 9:1 and different calcination temperatures, (b) in argon with the TiO<sub>2</sub>:N ratio of 9:1 and different calcination temperatures, (c) in air with different TiO<sub>2</sub>:N ratios and calcined at 600 °C, (d) in argon with different TiO<sub>2</sub>:N ratios and calcined at 600 °C.

On a basis of the UV-Vis/DR spectra, the band gap energy of the photocatalysts was determined. Anatase is reported as an indirect band gap semiconductor, while rutile is assumed to be a direct band gap semiconductor [75,76]. Since the obtained photocatalysts contained, in general, both phases, the  $E_g$  values were calculated for the direct and indirect transitions alike. The results are presented in Table 1. A similar approach for calculating the  $E_g$  for both transitions appeared in other reports [77–80]. It can be observed that the  $E_g$  values were lower for the indirect transitions compared to the direct ones, which is in agreement with the literature [79,81]. Furthermore, the obtained indirect  $E_g$  values for the photocatalysts calcined in the air atmosphere at 500, 600, 700 and 800 °C were slightly higher compared to those calculated for the photocatalysts treated in argon. Generally, with the increasing calcination temperature, the band gap energy was slightly decreasing for both calcination atmospheres. The greatest decrease in the band gap energy for B-9-1-P-800, B-9-1-Ar-700 and B-9-1-Ar-800 was associated with high content of the rutile phase in these photocatalysts. Moreover, it can be observed that the band gap energy slightly decreased with an increasing amount of biuret. Hence, it can be concluded that the presence of C and N in TiO<sub>2</sub> contributed to the lowering of the band gap energy of the photocatalyst. On the other hand, the apparent relationship between sulfur content and  $E_g$  was not observed. Nonetheless, the obtained results revealed that the non-metals content had less impact on the band gap energy value than the crystalline composition of the photocatalysts.

The modified photocatalysts were also characterized with reference to their surface charge. Table 1 presents the determined pH(I) values. When pH is below the pH(I), the photocatalyst surface is positively charged and reversely, when pH is over the pH(I) value, the photocatalyst surface is negatively charged [82,83]. The pH(I) values of the prepared photocatalysts were found to range from 3.6 to 6.4. An increase in the calcination temperature shifts the pH(I) to the lower values [84,85]. Furthermore, the low values of pH(I) are highly associated with lowering amount of the hydroxyl groups on the photocatalyst surface during the calcination process [86]. For the photocatalysts consisting mostly of anatase phase, the pH(I) ranged from 4.5 to 6.4. In that case, no significant effect of the pH(I) on the adsorption capacity towards ketoprofen was found (0.41 to 0.52 mg/g). However, the photocatalysts containing more rutile phase had significantly lower pH(I) of 3.6 and 3.9

for B-9-1-P-800 and B-9-1-Ar-800, respectively. The adsorption capacity in this case was also apparently lower and equaled to 0.18 mg/g for both photocatalysts.

### 3.2. Effect of Calcination Atmosphere and Temperature on the Photocatalytic Activity

Two series of the photocatalysts were prepared with the  $\text{TiO}_2\text{:N}$  ratio of 9:1. One of them was calcined for 1 h in the air and the other in argon atmosphere at 4 different temperatures of 500, 600, 700 and 800 °C. The influence of the atmosphere and temperature was investigated during photocatalytic decomposition of ketoprofen under simulated solar light. The degree of mineralization was evaluated by TOC removal after 24 h of the experiment. The results are shown in Figure 4.

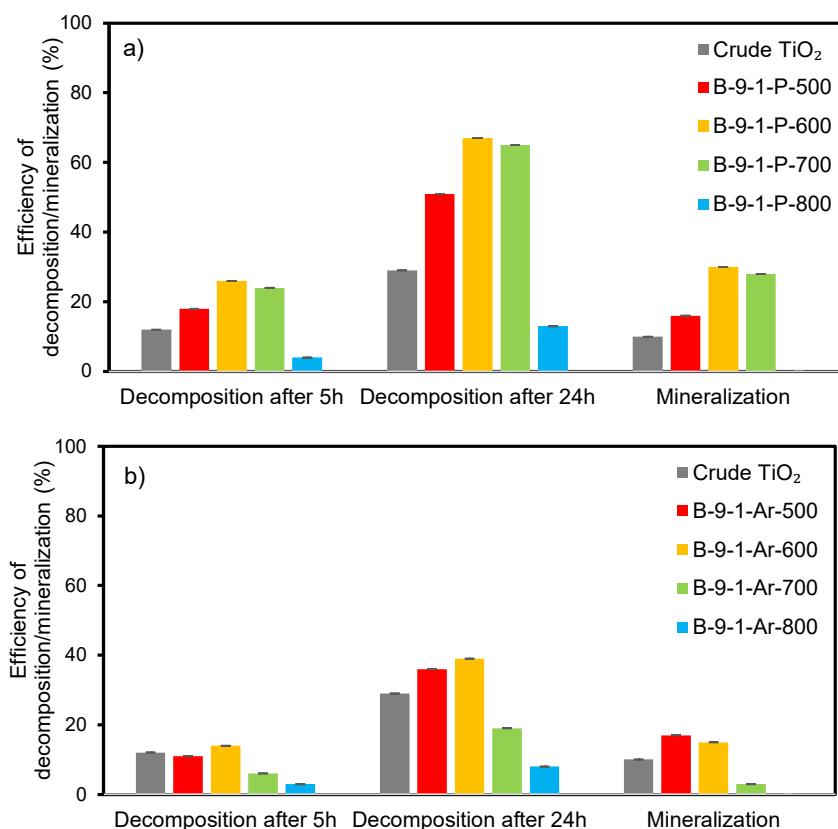


**Figure 4.** Effect of calcination temperature on the photocatalytic degradation of ketoprofen under simulated solar light in the presence of the photocatalysts prepared in (a) air and (b) argon.

It can be observed that the highest photoactivity towards ketoprofen decomposition after 5 and 24 h of photocatalysis revealed the photocatalysts calcined at 600 and 700 °C in air and at 500 and 600 °C in argon, respectively. The B-9-1-P-600 and B-9-1-P-700 showed very similar efficiency of ketoprofen decomposition (67% and 65% after 24 h, respectively) and mineralization (30% and 28% after 24 h). The B-9-1-Ar-500 and B-9-1-Ar-600 photocatalysts calcined in the argon atmosphere also exhibited similar activity to each other (36% and 39% decomposition, and 17% and 15% mineralization efficiency after 24 h, respectively). Conversely, for photocatalysts calcined in argon at 600 and 700 °C, the discrepancies in photocatalytic activity were significant. The B-9-1-Ar-700 showed only 19% decomposition and 3% mineralization efficiency after 24 h of photocatalysis. For both series of the photocatalysts, those treated at 600 °C displayed the highest ketoprofen decomposition rate. This can be attributed to the high content of anatase phase (ca. 95%) with crystallite size of about 25 nm in these photocatalysts. Nonetheless, the photodecomposition rate was significantly higher in the case of B-9-1-P-600 photocatalyst calcined in air (67% after 24 h) compared to B-9-1-Ar-600 treated in argon (39%) indicating that other factors than crystallinity are also important. The removal rate for B-9-1-Ar-700 was even lower than for

crude  $\text{TiO}_2$  (29% decomposition and 10% mineralization efficiency after 24 h), which was due to the substantial content of rutile phase (60.1%). Yet, worse results were obtained for B-9-1-Ar-800 (8% decomposition efficiency after 24 h and no mineralization), consisting of even more rutile phase (97.5%). Similarly, the photocatalyst calcined at 800 °C in air, containing 97.3% of rutile, showed removal efficiency lower (13% after 24 h) than crude  $\text{TiO}_2$ . Moreover, the experiments with the use of the photocatalysts treated at 800 °C were the only ones from both series where no mineralization occurred at all. This was due to the very low content of anatase phase in these photocatalysts. Good photocatalytic activity was found to be highly associated with anatase crystallites size. For both series of photocatalysts, there was a noticeable relationship between crystallites size and ketoprofen decomposition efficiency. The size of about 25 nm was revealed to be the most favorable (23 nm for B-9-1-P-600 and 26 nm for B-9-1-Ar-600). Below and above this size, the decomposition efficiency was decreasing.

The results (Table 1) clearly show that the increase in calcination temperature, regardless of the calcination atmosphere, contributed to the decrease in nitrogen and sulfur content in the photocatalysts. Conversely, this relationship was not so apparent for carbon. Overall, both series of photocatalysts showed a decrease in carbon content with increasing temperature. However, among the photocatalysts calcined in air, the one treated at 800 °C had more carbon than the photocatalyst annealed at 700 °C. In turn, among photocatalysts calcined in argon, the photocatalyst treated at 600 °C had the highest carbon content of 0.07 wt%. Of the non-metals, sulfur, in particular, seemed to have a high impact on the photocatalytic activity. The photocatalysts from the series calcined in air were characterized by a significantly higher sulfur content than the photocatalysts calcined in argon. Moreover, they showed a much higher efficiency of ketoprofen decomposition and mineralization. In turn, nitrogen had less impact on ketoprofen decomposition efficiency in terms of photocatalysts from these series. It can be seen in the example of B-9-1-P-500 and B-9-1-Ar-500 photocatalysts, containing the same amount of nitrogen of 0.06 wt%. The B-9-1-Ar-500 showed ca. 30% lower decomposition efficiency than B-9-1-P-500. However, it did not affect mineralization, which was very similar for both photocatalysts. Carbon also seemed to have lower influence on ketoprofen decomposition efficiency. This can be seen on an example of B-9-1-P-600 photocatalyst, showing similar photoactivity as B-9-1-P-700, while having more than twice the amount of carbon.

The research leads to the conclusion that the anatase phase content in the photocatalyst and anatase crystallite size are crucial for its photocatalytic properties. The most beneficial anatase phase content and anatase crystallite size were obtained at the temperature of 600 °C, regardless of the calcination atmosphere. However, using the air atmosphere provided higher photocatalytic activity during ketoprofen decomposition than using the argon atmosphere. This can be related to the generally higher non-metals content in photocatalysts calcined in air than in argon. Among the applied non-metals, sulfur was found to have the greatest impact on the photocatalytic activity.

### 3.3. Effect of Biuret Dose on the Photocatalytic Activity

Different ratios of  $\text{TiO}_2$ :N were applied to study the effect of the biuret dose on the photocatalytic activity. The as-prepared photocatalysts were compared at the preselected, most-beneficial calcination temperature of 600 °C in both, air and argon atmosphere. The results are presented in Figure 5.

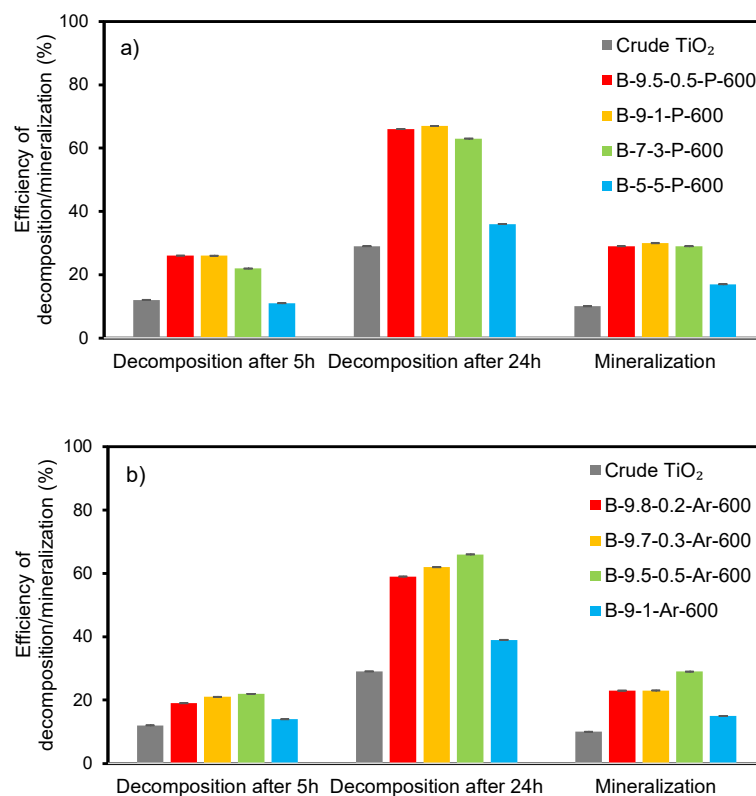


**Figure 5.** Effect of the biuret dose on photocatalytic degradation of ketoprofen under simulated solar light in the presence of the photocatalysts prepared in (a) air and (b) argon.

For the photocatalysts with different TiO<sub>2</sub>:N ratios calcined in air, the ketoprofen removal efficiency was in the range of 22–26% after 5 h and 63–67% after 24 h of irradiation, respectively. A 28–30% mineralization was observed after 24 h of experiment. The photocatalysts prepared with a low amount of biuret (B-9.5-0.5-P-600 and B-9-1-P-600) showed a slightly higher activity than the photocatalysts prepared with a higher addition of biuret (B-7-3-P-600 and B-5-5-P-600). Among photocatalysts calcined in the argon atmosphere, the B-9-1-Ar-600 prepared with the application of the highest biuret amount showed the lowest activity reaching only 14% of ketoprofen removal after 5 h and 39% after 24 h. The photocatalysts with TiO<sub>2</sub>:N ratio of 9.8:0.2, 9.7:0.3 and 9.5:0.5 exhibited the ketoprofen removal efficiency of 19–22% after 5 h and 59–66% after 24 h of irradiation, respectively. Mineralization efficiency after 24 h was 15% for B-9-1-Ar-600, while being 23% for B-9.8-0.2-Ar-600 and B-9.7-0.3-Ar-600. In the presence of the most efficient photocatalysts of this series (B-9.5-0.5-Ar-600) a 29% mineralization efficiency was achieved, which was almost two times higher than observed for B-9-1-Ar-600 and almost three times more than that of the crude TiO<sub>2</sub>.

Among the photocatalysts calcined in air, the B-9-1-P-600 showed the greatest photocatalytic activity, reaching 67% ketoprofen decomposition and 30% mineralization efficiency after 24 h of photocatalysis. Conversely, among the photocatalysts calcined in the argon atmosphere, the most effective B-9.5-0.5-Ar-600 reached 66% ketoprofen decomposition and 29% mineralization efficiency after 24 h of the process. These results can be explained by a similar crystalline structure of both photocatalysts (Table 1), as well as by a similar content of the non-metals. The B-9-1-P-600 had C, N and S content of 0.11, 0.05 and 0.77 wt%, respectively, whereas the B-9.5-0.5-Ar-600 contained 0.07, 0.02 and 0.83 wt% of C, N and S, respectively. Instead, the lowest photocatalytic activity in each series was observed for B-5-5-P-600 and B-9-1-Ar-600. Both photocatalysts exhibited similar phase composition. The anatase to rutile ratio of these photocatalysts were 94.3:5.7 and 94.6:5.4, respectively. The B-5-5-P-600 was characterized by the C, N and S content of 0.19, 0.16 and

0.33 wt%, whereas in the case of the B-9-1-Ar-600 the C, N and S content was 0.07, 0.03 and 0.10 wt%, respectively. This indicates that the amount of sulfur had the major influence on the photocatalytic activity of the non-metal doped photocatalysts. Moreover, the research results suggested that the most beneficial sulfur content was ca. 0.80% (Table 1), which is in agreement with the previous literature reports. Khang et al. [87] examined several photocatalysts with different S content and achieved the best photocatalytic activity for the photocatalysts containing 0.80% S.

For both series of the photocatalysts, lowering of the  $E_g$  value was not directly related to the improvement of the photocatalytic activity. However, some influence of the  $E_g$  can be observed based on the very similar values calculated for the most and the least efficient photocatalyst of each series. The indirect  $E_g$  value for the most efficient B-9-1-P-600 and B-9.5-0.5-Ar-600 amounted to 3.26 eV. In turn, the indirect  $E_g$  value for the least efficient B-5-5-P-600 and B-9-1-Ar-600 equaled to 3.21 eV. Nonetheless, in general, the decrease in the band gap did not contribute to the improvement of photoactivity.

On the basis of the obtained results, it can be concluded that the calcination temperature has a more significant impact on the efficiency of ketoprofen decomposition and mineralization than biuret dosage. This suggests that the main role in photocatalytic activity can be assigned to the anatase to rutile phase ratio and anatase crystallites size. Moreover, it was proved that sulfur content also played an important role in terms of the ketoprofen decomposition efficiency.

### 3.4. Effect of the Irradiation Type on the Photocatalytic Activity

Selected photocatalysts from each series were examined in the photocatalytic decomposition of ketoprofen under simulated solar light, visible light and UV. The photocatalysts were chosen based on the highest ketoprofen decomposition efficiency from each series out of the photocatalysts: (i) with the  $\text{TiO}_2$ :N ratio of 9:1, calcined at different temperatures in the air atmosphere, (ii) with the  $\text{TiO}_2$ :N ratio of 9:1, calcined at different temperatures in the argon atmosphere, (iii) with different  $\text{TiO}_2$ :N ratios, calcined at 600 °C in the air atmosphere and (iv) with different  $\text{TiO}_2$ :N ratios, calcined at 600 °C in the argon atmosphere.

Figure 6 presents the plots of  $-\ln(c_t/c_0)$  vs time applied for the calculation of the rate constants ( $k$ ). A linear dependence can be noticed for all photocatalysts. Table 2 summarizes the results of the calculations. The photoactivity of the photocatalysts examined under simulated solar light and UV followed the order: B-9-1-P-600 > B-9.5-0.5-Ar-600 > B-9-1-Ar-600 > crude  $\text{TiO}_2$ , whereas for the visible light they followed the order: B-9-1-P-600 > B-9-1-Ar-600 > B-9.5-0.5-Ar-600 > crude  $\text{TiO}_2$ . For the photocatalysts B-9-1-P-600, B-9-1-Ar-600 and B-9.5-0.5-Ar-600 irradiated with visible light, the rate constants were, respectively, ca. 2.8, 2.3 and 2.2 times higher than for the crude  $\text{TiO}_2$  ( $k = 0.0048 \text{ h}^{-1}$ ). However, for these photocatalysts tested under UV light, the  $k$  values were, respectively, ca. 2.5, 1.6 and 1.9 times higher than for crude  $\text{TiO}_2$  ( $k = 0.3511 \text{ h}^{-1}$ ). The reason could be that non-metal doping of  $\text{TiO}_2$  enhanced photocatalytic activity in the visible light more than in UV [88].

In the case of the visible light experiment, the obtained  $k$  values for B-9-1-Ar-600 and B-9.5-0.5-Ar-600 were very similar and equaled to 0.0109 and 0.0106  $\text{h}^{-1}$ , respectively. Moreover, the C and N content in these photocatalysts was also very similar and amounted to 0.07 wt% of C and 0.02–0.03 wt% of N. In turn, for the B-9-1-P-600 the  $k$  value was 0.0136  $\text{h}^{-1}$ , while C and N content was 0.11 and 0.05 wt%, respectively. With increasing C and N content, an increase in  $k$  value can be observed. Hence, it can be concluded that C and N doping of the photocatalyst had a positive influence on the photoactivity in visible light. On the other hand, S seemed to have less impact on the  $k$  value under visible light irradiation, since the B-9-1-Ar-600 and B-9.5-0.5-Ar-600 had significantly different S content of 0.10 and 0.83 wt%, respectively, while having almost equal  $k$  values. Nevertheless, S content apparently played an important role in terms of  $k$  value under simulated solar light. In the case of the photocatalysts B-9-1-P-600 (0.77 wt% of S) and B-9.5-0.5-Ar-600 (0.83 wt% of S), the  $k$  value was much higher (0.0636 and 0.0498  $\text{h}^{-1}$ , respectively), than

for B-9-1-Ar-600, having 0.10 wt% of S ( $k = 0.0303 \text{ h}^{-1}$ ). The  $k$  value of B-9-1-Ar-600 under simulated solar light was only slightly higher than the  $k$  of the crude  $\text{TiO}_2$  ( $k = 0.0291 \text{ h}^{-1}$ ).

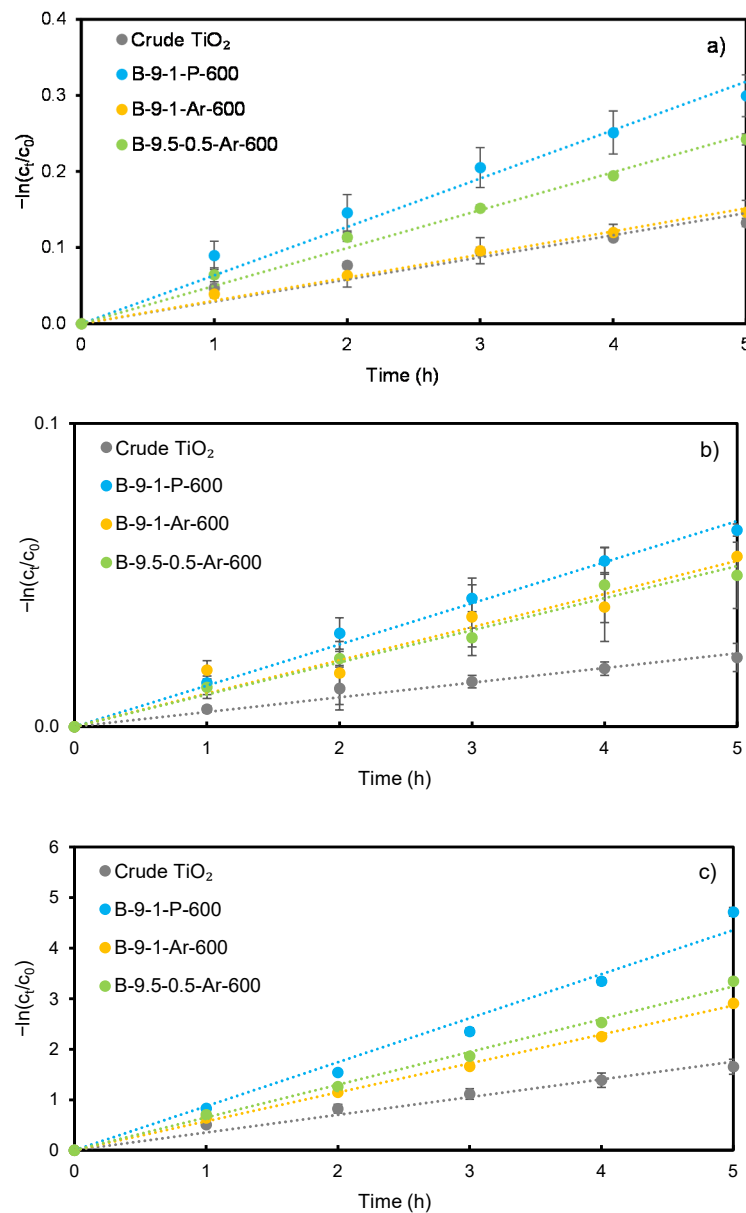


**Figure 6.** Kinetic study of ketoprofen degradation over crude  $\text{TiO}_2$  and selected non-metal doped photocatalysts under (a) simulated solar light, (b) visible light and (c) UV.

**Table 2.** Apparent pseudo-first-order rate constant  $k$  ( $\text{h}^{-1}$ ) of ketoprofen decomposition under simulated solar light ( $k_{\text{ss}}$ ), visible light ( $k_{\text{vis}}$ ) and UV ( $k_{\text{UV}}$ ) in the presence of crude  $\text{TiO}_2$  and selected photocatalysts.

Photocatalyst	$k_{\text{ss}}$	$R^2_{\text{ss}}$	$k_{\text{vis}}$	$R^2_{\text{vis}}$	$k_{\text{UV}}$	$R^2_{\text{UV}}$
Crude $\text{TiO}_2$	0.0291	0.981	0.0048	0.991	0.3511	0.992
B-9-1-P-600	0.0636	0.993	0.0136	0.997	0.8715	0.994
B-9-1-Ar-600	0.0303	0.997	0.0109	0.984	0.5725	0.999
B-9.5-0.5-Ar-600	0.0498	0.997	0.0106	0.993	0.6485	0.999

The mineralization efficiency after 24 h under simulated solar light for B-9-1-P-600 and B-9.5-0.5-Ar-600 was almost equal and amounted to 30% and 29%, respectively. In turn, the

mineralization efficiency obtained for B-9-1-Ar-600 and the crude TiO<sub>2</sub> was 15% and 10%, respectively. Under visible light, only in the case of B-9-1-P-600, a slight mineralization of 2% after 24 h was observed, while in the case of the other photocatalyst, the mineralization did not occur at all. Comparatively, under UV irradiation, the mineralization efficiency after 5 h for B-9-1-P-600, B-9-1-Ar-600 and B-9.5-0.5-Ar-600 was 64%, 51% and 50%, respectively, while for the crude TiO<sub>2</sub> it was 21%.

The obtained results revealed that the C, N and S content had some impact on the mineralization efficiency under simulated solar light, what can be found in the case of B-9.5-0.5-Ar-600, having almost two times higher photoactivity than B-9-1-Ar-600. Conversely, these two photocatalysts showed similar mineralization efficiency under UV light, indicating that the non-metals content did not play a significant role in this type of irradiation. Under visible light the mineralization occurred only in the case of B-9-1-P-600, which contained the highest amount of non-metals among the selected photocatalysts. These results are consistent with the mechanisms of photocatalysis with non-metal doped TiO<sub>2</sub> [37]. In the case of UV-induced photocatalysis, the photon energy was sufficient for the excitation of an electron from the VB to the CB, while in the case of visible and simulated solar-light-induced photocatalysis, the non-metal dopants played an essential role. Nevertheless, in every considered case, regardless the irradiation type, the photocatalyst B-9-1-P-600 had higher photoactivity during ketoprofen decomposition and mineralization than the selected, most-efficient photocatalysts calcined in the argon atmosphere. Hence, the application of the air atmosphere during the calcination process was proved to be favorable in terms of the photocatalytic activity of the prepared photocatalysts.

#### 4. Conclusions

Simple wet impregnation-calcination approach was used to obtain new non-metals modified TiO<sub>2</sub> photocatalysts active under simulated solar light. Raw titanium dioxide derived from sulfate technology process was used as TiO<sub>2</sub> and S source, while biuret was applied as C and N source. The photocatalytic activity was determined on a basis of decomposition and mineralization of ketoprofen, being a representative of NSAIDs. Comparing the photoactivity of the photocatalysts calcined at 500–800 °C, it was proved that the treatment in air resulted in a higher efficiency of ketoprofen decomposition than calcination in the argon atmosphere. The most active photocatalysts were obtained at the calcination temperature of 600 °C. It was concluded that the compromise between anatase to rutile phase ratio and the anatase crystallite size were essential features of the photocatalysts. The highest ketoprofen decomposition efficiency was observed for the photocatalyst characterized by the anatase to rutile ratio of 96.4:3.6 and anatase crystallites of 23 nm in size. Nevertheless, the presence of the non-metals in the TiO<sub>2</sub> structure also had an influence on the photocatalytic activity of the prepared photocatalysts. It was revealed that among C, N and S, the sulfur played a major role in terms of photocatalytic properties, in particular, in the case of simulated solar light. The most beneficial content of S was 0.77 wt%. In turn, C and N played a major role when visible light photocatalysis was considered. The most advantageous amounts of C and N were 0.11 and 0.05 wt%, respectively. It was also observed that the band gap energy did not show as significant an impact on the photocatalytic activity of the prepared photocatalysts as the other examined factors.

**Author Contributions:** Conceptualization, A.P. and S.M.; methodology, A.P. and S.M.; investigation, A.P.; writing—original draft preparation, A.P. and S.M.; visualization, A.P.; supervision, S.M.; funding acquisition, S.M. All authors have read and agreed to the published version of the manuscript.

**Funding:** This work was supported by the National Science Centre, Poland under project No. 2019/33/B/ST8/00252.

**Data Availability Statement:** The data that support the findings of this study are available from the corresponding author upon reasonable request.

**Acknowledgments:** Authors thank Dominika Darowna for performing isoelectric point measurement and Marcin Sadłowski for XRD analysis.

**Conflicts of Interest:** The authors declare no conflict of interest.

## References

1. Saeed, A.A.H.; Harun, N.Y.; Sufian, S.; Aznan, M.F.B. Effect of adsorption parameter on the removal of nickel (II) by low-cost adsorbent extracted from corn cob. *IJARET* **2020**, *11*, 981–989. [[CrossRef](#)]
2. Patel, M.; Kumar, R.; Kishor, K.; Mlsna, T.; Pittman, C.U., Jr.; Mohan, D. Pharmaceuticals of emerging concern in aquatic systems: Chemistry, occurrence, effects, and removal methods. *Chem. Rev.* **2019**, *119*, 3510–3673. [[CrossRef](#)]
3. Ojemaye, C.Y.; Petrik, L. Pharmaceuticals in the marine environment: A review. *Environ. Rev.* **2019**, *27*, 151–165. [[CrossRef](#)]
4. Rivera-Utrilla, J.; Sánchez-Polo, M.; Ferro-García, M.Á.; Prados-Joya, G.; Ocampo-Pérez, R. Pharmaceuticals as emerging contaminants and their removal from water. A review. *Chemosphere* **2013**, *93*, 1268–1287. [[CrossRef](#)]
5. Cai, Z.; Dwivedi, A.D.; Lee, W.-N.; Zhao, X.; Liu, W.; Sillanpää, M.; Zhao, D.; Huang, C.-H.; Fu, J. Application of nanotechnologies for removing pharmaceutically active compounds from water: Development and future trends. *Environ. Sci. Nano* **2018**, *5*, 27–47. [[CrossRef](#)]
6. Kanakaraju, D.; Glass, B.D.; Oelgemöller, M. Advanced oxidation process-mediated removal of pharmaceuticals from water: A review. *J. Environ. Manag.* **2018**, *219*, 189–207. [[CrossRef](#)]
7. Mlunguza, N.Y.; Ncube, S.; Nokwethemba Mahlambi, P.; Chimuka, L.; Madikizela, L.M. Adsorbents and removal strategies of non-steroidal anti-inflammatory drugs from contaminated water bodies. *J. Environ. Chem. Eng.* **2019**, *7*, 103142. [[CrossRef](#)]
8. Williams, M.; Kookana, R.S.; Mehta, A.; Yadav, S.K.; Tailor, B.L.; Maheshwari, B. Emerging contaminants in a river receiving untreated wastewater from an indian urban centre. *Sci. Total. Environ.* **2019**, *647*, 1256–1265. [[CrossRef](#)]
9. Karimi-Maleh, H.; Ayati, A.; Davoodi, R.; Tanhaei, B.; Karimi, F.; Malekmohammadi, S.; Orooji, Y.; Fu, L.; Sillanpää, M. Recent advances in using of chitosan-based adsorbents for removal of pharmaceutical contaminants: A review. *J. Clean. Prod.* **2021**, *291*, 125880. [[CrossRef](#)]
10. Madikizela, L.M.; Chimuka, L. Occurrence of naproxen, ibuprofen, and diclofenac residues in wastewater and river water of Kwazulu-Natal Province in South Africa. *Environ. Monit. Assess.* **2017**, *189*, 348. [[CrossRef](#)]
11. Husk, B.; Sanchez, J.S.; Leduc, R.; Takser, L.; Savary, O.; Cabana, H. Pharmaceuticals and pesticides in rural community drinking waters of Quebec, Canada—A regional study on the susceptibility to source contamination. *Water Qual. Res. J.* **2019**, *54*, 88–103. [[CrossRef](#)]
12. Gumbi, B.P.; Moodley, B.; Birungi, G.; Ndungu, P.G. Assessment of nonsteroidal anti-inflammatory drugs by ultrasonic-assisted extraction and GC-MS in Mgeni and Msunduzi River sediments, KwaZulu-Natal, South Africa. *Environ. Sci. Pollut. Res.* **2017**, *24*, 20015–20028. [[CrossRef](#)]
13. Awfa, D.; Ateia, M.; Fujii, M.; Johnson, M.S.; Yoshimura, C. Photodegradation of pharmaceuticals and personal care products in water treatment using carbonaceous-TiO<sub>2</sub> composites: A critical review of recent literature. *Water Res.* **2018**, *142*, 26–45. [[CrossRef](#)]
14. Crini, G.; Lichtfouse, E. Advantages and disadvantages of techniques used for wastewater treatment. *Environ. Chem. Lett.* **2018**, *17*, 145–155. [[CrossRef](#)]
15. Garcia-Segura, S.; Brillas, E. Applied photoelectrocatalysis on the degradation of organic pollutants in wastewaters. *J. Photochem. Photobiol. C Photochem. Rev.* **2017**, *31*, 1–35. [[CrossRef](#)]
16. Banerjee, S.; Pillai, S.C.; Falaras, P.; O’Shea, K.E.; Byrne, J.A.; Dionysiou, D.D. New insights into the mechanism of visible light photocatalysis. *J. Phys. Chem. Lett.* **2014**, *5*, 2543–2554. [[CrossRef](#)]
17. Fujishima, A.; Zhang, X.; Tryk, D. TiO<sub>2</sub> photocatalysis and related surface phenomena. *Surf. Sci. Rep.* **2008**, *63*, 515–582. [[CrossRef](#)]
18. Lou, Q.; Li, H.; Huang, Q.; Shen, Z.; Li, F.; Du, Q.; Jin, M.; Chen, C. Multifunctional CNT:TiO<sub>2</sub> additives in Spiro-OMeTAD layer for highly efficient and stable perovskite solar cells. *EcoMat* **2021**, *3*, e12099. [[CrossRef](#)]
19. Wang, H.; Li, H.; Cai, W.; Zhang, P.; Cao, S.; Chen, Z.; Zang, Z. Challenges and strategies relating to device function layers and their integration toward high-performance inorganic perovskite solar cells. *Nanoscale* **2020**, *12*, 14369–14404. [[CrossRef](#)] [[PubMed](#)]
20. Yang, B.; Wang, M.; Hu, X.; Zhou, T.; Zang, Z. Highly efficient semitransparent CsPbI<sub>3</sub> Perovskite solar cells via low-temperature processed In<sub>2</sub>S<sub>3</sub> as electron-transport-layer. *Nano Energy* **2019**, *57*, 718–727. [[CrossRef](#)]
21. Khedr, T.M.; El-Sheikh, S.M.; Hakki, A.; Ismail, A.A.; Badawy, W.A.; Bahnmann, D.W. Highly active non-metals doped mixed-phase TiO<sub>2</sub> for photocatalytic oxidation of ibuprofen under visible light. *J. Photochem. Photobiol. A Chem.* **2017**, *346*, 530–540. [[CrossRef](#)]
22. Ramandi, S.; Entezari, M.H.; Ghows, N. Sono-synthesis of solar light responsive S–N–C–Tri doped TiO<sub>2</sub> photo-catalyst under optimized conditions for degradation and mineralization of diclofenac. *Ultrason. Sonochem.* **2017**, *38*, 234–245. [[CrossRef](#)]
23. Sanchez-Martinez, A.; Ceballos-Sanchez, O.; Koop-Santa, C.; López-Mena, E.R.; Orozco-Guareño, E.; García-Guaderrama, M. N-doped TiO<sub>2</sub> nanoparticles obtained by a facile coprecipitation method at low temperature. *Ceram. Int.* **2018**, *44*, 5273–5283. [[CrossRef](#)]
24. Nasirian, M.; Lin, Y.P.; Bustillo-Lecompte, C.F.; Mehrvar, M. Enhancement of Photocatalytic activity of titanium dioxide using non-metal doping methods under visible light: A review. *Int. J. Environ. Sci. Technol.* **2017**, *15*, 2009–2032. [[CrossRef](#)]
25. Mittal, A.; Mari, B.; Sharma, S.; Kumari, V.; Maken, S.; Kumari, K.; Kumar, N. Non-metal modified TiO<sub>2</sub>: A step towards visible light photocatalysis. *J. Mater. Sci. Mater. Electron.* **2019**, *30*, 3186–3207. [[CrossRef](#)]
26. Islam, S.; Nagpure, S.; Kim, D.; Rankin, S. Synthesis and catalytic applications of non-metal doped mesoporous titania. *Inorganics* **2017**, *5*, 15. [[CrossRef](#)]

27. Marques, J.; Gomes, T.D.; Forte, M.A.; Silva, R.F.; Tavares, C.J. A new route for the synthesis of highly-active N-doped TiO<sub>2</sub> nanoparticles for visible light photocatalysis using urea as nitrogen precursor. *Catal. Today* **2019**, *326*, 36–45. [[CrossRef](#)]
28. Chen, H.; Chen, K.-F.; Lai, S.-W.; Dang, Z.; Peng, Y.-P. Photoelectrochemical oxidation of azo dye and generation of hydrogen via CN co-doped TiO<sub>2</sub> nanotube arrays. *Sep. Purif. Technol.* **2015**, *146*, 143–153. [[CrossRef](#)]
29. Rengifo-Herrera, J.A.; Mielczarski, E.; Mielczarski, J.; Castillo, N.C.; Kiwi, J.; Pulgarin, C. Escherichia coli inactivation by N, S co-doped commercial TiO<sub>2</sub> powders under UV and visible light. *Appl. Catal. B Environ.* **2008**, *84*, 448–456. [[CrossRef](#)]
30. Albrbar, A.J.; Djokić, V.; Bjelajac, A.; Kovač, J.; Ćirković, J.; Mitrić, M.; Janačković, D.; Petrović, R. Visible-Light active mesoporous, nanocrystalline N,S-doped and co-doped titania photocatalysts synthesized by non-hydrolytic sol-gel route. *Ceram. Int.* **2016**, *42*, 16718–16728. [[CrossRef](#)]
31. Xiao, Y.; Sun, X.; Li, L.; Chen, J.; Zhao, S.; Jiang, C.; Yang, L.; Cheng, L.; Cao, S. Simultaneous formation of a C/N-TiO<sub>2</sub> hollow photocatalyst with efficient photocatalytic performance and recyclability. *Chin. J. Catal.* **2019**, *40*, 765–775. [[CrossRef](#)]
32. Zhang, J.; Huang, G.-F.; Li, D.; Zhou, B.-X.; Chang, S.; Pan, A.; Huang, W.-Q. Facile route to fabricate carbon-doped TiO<sub>2</sub> nanoparticles and its mechanism of enhanced visible light photocatalytic activity. *Appl. Phys. A* **2016**, *122*, 994. [[CrossRef](#)]
33. Qiu, B.; Zhong, C.; Xing, M.; Zhang, J. Facile preparation of C-modified TiO<sub>2</sub> supported on MCF for high visible-light-driven photocatalysis. *RSC Adv.* **2015**, *5*, 17802–17808. [[CrossRef](#)]
34. Saharudin, K.A.; Sreekantan, S.; Lai, C.W. Fabrication and photocatalysis of nanotubular C-doped TiO<sub>2</sub> arrays: Impact of annealing atmosphere on the degradation efficiency of methyl orange. *Mater. Sci. Semicond. Process.* **2014**, *20*, 1–6. [[CrossRef](#)]
35. Boningari, T.; Inturi, S.N.R.; Suidan, M.; Smirniotis, P.G. Novel one-step synthesis of nitrogen-doped TiO<sub>2</sub> by flame aerosol technique for visible-light photocatalysis: Effect of synthesis parameters and secondary nitrogen (N) source. *Chem. Eng. J.* **2018**, *350*, 324–334. [[CrossRef](#)]
36. Bento, R.T.; Correa, O.V.; Pillis, M.F. Photocatalytic activity of undoped and sulfur-doped TiO<sub>2</sub> films grown by MOCVD for water treatment under visible light. *J. Eur. Ceram. Soc.* **2019**, *39*, 3498–3504. [[CrossRef](#)]
37. Piątkowska, A.; Janus, M.; Szymański, K.; Mozia, S. C-, N- and S-Doped TiO<sub>2</sub> photocatalysts: A review. *Catalysts* **2021**, *11*, 144. [[CrossRef](#)]
38. Chaudhari, N.K.; Song, M.Y.; Yu, J.-S. Heteroatom-doped highly porous carbon from human urine. *Sci. Rep.* **2014**, *4*, 5221. [[CrossRef](#)]
39. Azami, M.S.; Nawawi, W.I.; Shukri, D.S.M. Formation of predominant interstitial N-TiO<sub>2</sub> using physical preparation under microwave irradiation for reactive red 4 dye removal. *Desalin. Water Treat.* **2017**, *92*, 172–180. [[CrossRef](#)]
40. Zhou, Y.; Liu, Y.; Liu, P.; Zhang, W.; Xing, M.; Zhang, J. A facile approach to further improve the substitution of nitrogen into reduced TiO<sub>2</sub>— with an enhanced photocatalytic activity. *Appl. Catal. B Environ.* **2015**, *170–171*, 66–73. [[CrossRef](#)]
41. Dawson, M.; Soares, G.B.; Ribeiro, C. Influence of calcination parameters on the synthesis of N-doped TiO<sub>2</sub> by the polymeric precursors method. *J. Solid State Chem.* **2014**, *215*, 211–218. [[CrossRef](#)]
42. Cao, Y.; Xing, Z.; Shen, Y.; Li, Z.; Wu, X.; Yan, X.; Zou, J.; Yang, S.; Zhou, W. Mesoporous black Ti<sup>3+</sup> /N-TiO<sub>2</sub> spheres for efficient visible-light-driven photocatalytic performance. *Chem. Eng. J.* **2017**, *325*, 199–207. [[CrossRef](#)]
43. Shaban, Y.A. Solar light-induced photodegradation of chrysene in seawater in the presence of carbon-modified n-TiO<sub>2</sub> nanoparticles. *Arab. J. Chem.* **2019**, *12*, 652–663. [[CrossRef](#)]
44. Di Valentin, C.; Pacchioni, G.; Selloni, A. Theory of carbon doping of titanium dioxide. *Chem. Mater.* **2005**, *17*, 6656–6665. [[CrossRef](#)]
45. Vorontsov, A.V.; Valdés, H. Insights into the visible light photocatalytic activity of s-doped hydrated TiO<sub>2</sub>. *Int. J. Hydrogen Energy* **2019**, *44*, 17963–17973. [[CrossRef](#)]
46. Bakar, S.A.; Ribeiro, C.A. Comparative run for visible-light-driven photocatalytic activity of anionic and cationic S-doped TiO<sub>2</sub> photocatalysts: A case study of possible sulfur doping through chemical protocol. *J. Mol. Catal. A Chem.* **2016**, *421*, 1–15. [[CrossRef](#)]
47. Ma, D.; Xin, Y.; Gao, M.; Wu, J. Fabrication and photocatalytic properties of cationic and anionic S-doped TiO<sub>2</sub> Nanofibers by electrospinning. *Appl. Catal. B Environ.* **2014**, *147*, 49–57. [[CrossRef](#)]
48. Boningari, T.; Inturi, S.N.R.; Suidan, M.; Smirniotis, P.G. Novel one-step synthesis of sulfur doped-TiO<sub>2</sub> by flame spray pyrolysis for visible light photocatalytic degradation of acetaldehyde. *Chem. Eng. J.* **2018**, *339*, 249–258. [[CrossRef](#)]
49. Ananpattarachai, J.; Seraphin, S.; Kajitvichyanukul, P. Formation of hydroxyl radicals and kinetic study of 2-chlorophenol photocatalytic oxidation using C-doped TiO<sub>2</sub>, N-doped TiO<sub>2</sub>, and C,N Co-doped TiO<sub>2</sub> under visible light. *Environ. Sci. Pollut. Res.* **2015**, *23*, 3884–3896. [[CrossRef](#)] [[PubMed](#)]
50. Chung, J.; Chung, J.W.; Kwak, S.-Y. Adsorption-assisted photocatalytic activity of nitrogen and sulfur codoped TiO<sub>2</sub> under visible light irradiation. *Phys. Chem. Chem. Phys.* **2015**, *17*, 17279–17287. [[CrossRef](#)] [[PubMed](#)]
51. Sushma, C.; Kumar, S.G. C–N–S tridoping into TiO<sub>2</sub> matrix for photocatalytic applications: Observations, speculations and contradictions in the codoping process. *Inorg. Chem. Front.* **2017**, *4*, 1250–1267. [[CrossRef](#)]
52. Kuang, L.; Zhang, W. Enhanced hydrogen production by carbon-doped TiO<sub>2</sub> decorated with reduced graphene oxide (RGO) under visible light irradiation. *RSC Adv.* **2016**, *6*, 2479–2488. [[CrossRef](#)]
53. Cheng, X.; Yu, X.; Xing, Z.; Yang, L. Synthesis and characterization of N-doped TiO<sub>2</sub> and its enhanced visible-light photocatalytic activity. *Arab. J. Chem.* **2016**, *9*, S1706–S1711. [[CrossRef](#)]

54. Romanovska, N.I.; Manoryk, P.A.; Selyshchev, O.V.; Ermokhina, N.I.; Yaremov, P.S.; Grebennikov, V.M.; Shcherbakov, S.M.; Zahn, D.R.T. Effect of the modification of TiO<sub>2</sub> with thiourea on its photocatalytic activity in doxycycline degradation. *Theor. Exp. Chem.* **2020**, *56*, 183–191. [[CrossRef](#)]
55. Ji, L.; Zhou, S.; Liu, X.; Gong, M.; Xu, T. Synthesis of carbon- and nitrogen-doped TiO<sub>2</sub>/carbon composite fibers by a surface-hydrolyzed PAN fiber and their photocatalytic property. *J. Mater. Sci.* **2019**, *55*, 2471–2481. [[CrossRef](#)]
56. Meng, Q.; Liu, B.; Liu, H.; Cai, Y.; Dong, L. Effects of S and Ta codoping on photocatalytic activity of rutile TiO<sub>2</sub>. *J. Sol-Gel Sci. Technol.* **2018**, *86*, 631–639. [[CrossRef](#)]
57. Koltsakidou, A.; Antonopoulou, M.; Evgenidou, E.; Konstantinou, I.; Giannakas, A.E.; Papadaki, M.; Bikiaris, D.; Lambropoulou, D.A. Photocatalytical removal of fluorouracil using TiO<sub>2</sub>-P25 and N/S doped TiO<sub>2</sub> catalysts: A kinetic and mechanistic study. *Sci. Total Environ.* **2017**, *578*, 257–267. [[CrossRef](#)]
58. Zhao, W.; Liu, S.; Wang, R.; Du, H. Effect of calcination atmospheres on visible light photocatalytic performance of N-TiO<sub>2</sub>. *Chin. J. Environ. Eng.* **2019**, *13*, 2907–2914. [[CrossRef](#)]
59. Xia, Y.; Jiang, Y.; Li, F.; Xia, M.; Xue, B.; Li, Y. Effect of calcined atmosphere on the photocatalytic activity of P-doped TiO<sub>2</sub>. *Appl. Surf. Sci.* **2014**, *289*, 306–315. [[CrossRef](#)]
60. Hu, M.; Fang, M.; Tang, C.; Yang, T.; Huang, Z.; Liu, Y.; Wu, X.; Min, X. The effects of atmosphere and calcined temperature on photocatalytic activity of TiO<sub>2</sub> nanofibers prepared by electrospinning. *Nanoscale Res. Lett.* **2013**, *8*, 548. [[CrossRef](#)]
61. Văcăroiu, C.; Enache, M.; Gartner, M.; Popescu, G.; Anastasescu, M.; Brezeanu, A.; Todorova, N.; Giannakopoulou, T.; Trapalis, C.; Dumitru, L. The effect of thermal treatment on antibacterial properties of nanostructured TiO<sub>2</sub>(N) films illuminated with visible light. *World J. Microbiol. Biotechnol.* **2008**, *25*, 27–31. [[CrossRef](#)]
62. Yamada, K.; Yamane, H.; Matsushima, S.; Nakamura, H.; Ohira, K.; Kouya, M.; Kumada, K. Effect of thermal treatment on photocatalytic activity of N-doped TiO<sub>2</sub> particles under visible light. *Thin Solid Films* **2008**, *516*, 7482–7487. [[CrossRef](#)]
63. Patterson, A.L. The scherrer formula for X-ray particle size determination. *Phys. Rev.* **1939**, *56*, 978–982. [[CrossRef](#)]
64. Weibel, A.; Bouchet, R.; Boulc', F.; Knauth, P. The big problem of small particles: A comparison of methods for determination of particle size in nanocrystalline anatase powders. *Chem. Mater.* **2005**, *17*, 2378–2385. [[CrossRef](#)]
65. Makuła, P.; Pacia, M.; Macyk, W. How to correctly determine the band gap energy of modified semiconductor photocatalysts based on UV-Vis spectra. *J. Phys. Chem. Lett.* **2018**, *9*, 6814–6817. [[CrossRef](#)]
66. Grabowska, E.; Reszczyńska, J.; Zaleska, A. Retracted: Mechanism of phenol photodegradation in the presence of pure and modified-TiO<sub>2</sub>: A review. *Water Res.* **2012**, *46*, 5453–5471. [[CrossRef](#)] [[PubMed](#)]
67. Hanaor, D.A.H.; Sorrell, C.C. Review of the anatase to rutile phase transformation. *J. Mater. Sci.* **2010**, *46*, 855–874. [[CrossRef](#)]
68. Czanderna, A.W.; Rao, C.N.R.; Honig, J.M. The anatase-rutile transition. Part 1.—Kinetics of the transformation of pure anatase. *Trans. Faraday Soc.* **1958**, *54*, 1069–1073. [[CrossRef](#)]
69. Albetran, H.; Low, I.M. Parameters controlling the crystallization kinetics of nanostructured TiO<sub>2</sub>—An overview. *Mater. Today Proc.* **2019**, *16*, 25–35. [[CrossRef](#)]
70. Albetran, H.; O'Connor, B.H.; Low, I.M. Effect of calcination on band gaps for electrospun titania nanofibers heated in air-argon mixtures. *Mater. Des.* **2016**, *92*, 480–485. [[CrossRef](#)]
71. Amores, J.M.G.; Escibano, V.S.; Busca, G. Anatase crystal growth and phase transformation to rutile in high-area TiO<sub>2</sub>, MoO<sub>3</sub>-TiO<sub>2</sub> and other TiO<sub>2</sub>-supported oxide catalytic systems. *J. Mater. Chem.* **1995**, *5*, 1245–1249. [[CrossRef](#)]
72. Ding, X.-Z.; Liu, X.-H. Correlation between anatase-to-rutile transformation and grain growth in nanocrystalline titania powders. *J. Mater. Res.* **1998**, *13*, 2556–2559. [[CrossRef](#)]
73. Helmy, E.T.; Nemr, A.E.; Arafa, E.; Eldafrawy, S.; Mousa, M. Photocatalytic degradation of textile dyeing wastewater under visible light irradiation using green synthesized mesoporous non-metal-doped TiO<sub>2</sub>. *Bull. Mater. Sci.* **2021**, *44*, 30. [[CrossRef](#)]
74. Cui, X.; Liu, H.; Zhang, X.; Liu, H. Macroporous-mesoporous C-, S-, N-doped titania microspheres via the PolyHIPE microspheres templates. *Chin. Chem. Lett.* **2021**, *32*, 1135–1138. [[CrossRef](#)]
75. Banerjee, S.; Gopal, J.; Muraleedharan, P.; Tyagi, A.K.; Raj, B. Physics and chemistry of photocatalytic titanium dioxide: Visualization of bactericidal activity using atomic force microscopy. *Curr. Sci.* **2006**, *90*, 1378–1383.
76. Zhang, J.; Zhou, P.; Liu, J.; Yu, J. New understanding of the difference of photocatalytic activity among anatase, rutile and brookite TiO<sub>2</sub>. *Phys. Chem. Chem. Phys.* **2014**, *16*, 20382–20386. [[CrossRef](#)]
77. Horti, N.C.; Kamatagi, M.D.; Patil, N.R.; Nataraj, S.K.; Sannaikar, M.S.; Inamdar, S.R. Synthesis and photoluminescence properties of titanium oxide (TiO<sub>2</sub>) nanoparticles: Effect of calcination temperature. *Optik* **2019**, *194*, 163070. [[CrossRef](#)]
78. Loan, T.T.; Huong, V.H.; Huyen, N.T.; Van Quyet, L.; Bang, N.A.; Long, N.N. Anatase to rutile phase transformation of iron-doped titanium dioxide nanoparticles: The role of iron content. *Opt. Mater.* **2021**, *111*, 110651. [[CrossRef](#)]
79. Jahdi, M.; Mishra, S.B.; Nxumalo, E.N.; Mhlanga, S.D.; Mishra, A.K. Synergistic effects of sodium fluoride (NaF) on the crystallinity and band gap of Fe-doped TiO<sub>2</sub> developed via microwave-assisted hydrothermal treatment. *Opt. Mater.* **2020**, *104*, 109844. [[CrossRef](#)]
80. Gupta, S.K.; Singh, J.; Anbalagan, K.; Kothari, P.; Bhatia, R.R.; Mishra, P.K.; Manjuladevi, V.; Gupta, R.K.; Akhtar, J. Synthesis, Phase to Phase Deposition and Characterization of Rutile Nanocrystalline Titanium dioxide (TiO<sub>2</sub>) thin films. *Appl. Surf. Sci.* **2013**, *264*, 737–742. [[CrossRef](#)]
81. Pyachin, S.A.; Burkov, A.A.; Makarevich, K.S.; Zaitsev, A.V.; Karpovich, N.F.; Ermakov, M.A. Optical characteristics of particles produced using electroerosion dispersion of titanium in hydrogen peroxide. *Tech. Phys.* **2016**, *61*, 1046–1052. [[CrossRef](#)]

82. Suttiponparnit, K.; Jiang, J.; Sahu, M.; Suvachittanont, S.; Charinpanitkul, T.; Biswas, P. Role of surface area, primary particle size, and crystal phase on titanium dioxide nanoparticle dispersion properties. *Nanoscale Res. Lett.* **2011**, *6*, 27. [[CrossRef](#)] [[PubMed](#)]
83. Park, H.; Yang, D.-J.; Yoo, J.-S.; Mun, K.-S.; Kim, W.-R.; Kim, H.-G.; Choi, W.-Y. Surface passivation of highly ordered TiO<sub>2</sub> nanotube arrays and application to dye-sensitized solar cells using the concept of isoelectric point. *J. Ceram. Soc. Jpn.* **2009**, *117*, 596–599. [[CrossRef](#)]
84. Cheng, P.; Li, W.; Zhou, T.; Jin, Y.; Gu, M. Physical and photocatalytic properties of zinc ferrite doped titania under visible light irradiation. *J. Photochem. Photobiol. A Chem.* **2004**, *168*, 97–101. [[CrossRef](#)]
85. Furlong, D.N.; Parfitt, G.D. Electrokinetics of titanium dioxide. *J. Colloid Interface Sci.* **1978**, *65*, 548–554. [[CrossRef](#)]
86. Tran, T.H.; Nosaka, A.Y.; Nosaka, Y. Adsorption and photocatalytic decomposition of amino acids in TiO<sub>2</sub> photocatalytic systems. *J. Phys. Chem. B* **2006**, *110*, 25525–25531. [[CrossRef](#)]
87. Khang, N.C.; Van, D.Q.; Thuy, N.M.; Minh, N.V.; Minh, P.N. Remarkably enhanced photocatalytic activity by sulfur-doped titanium dioxide in nanohybrids with carbon nanotubes. *J. Phys. Chem. Solids* **2016**, *99*, 119–123. [[CrossRef](#)]
88. Buda, W.; Czech, B. Preparation and characterization of C,N-Codoped TiO<sub>2</sub> photocatalyst for the Degradation of diclofenac from wastewater. *Water Sci. Technol.* **2013**, *68*, 1322–1328. [[CrossRef](#)]